

Scattering of SV waves by a canyon in a fluid-saturated, poroelastic layered half-space, modeled using the indirect boundary element method

Jianwen Liang^{a,*}, Hongbing You^a, Vincent W. Lee^b

^a*Department of Civil Engineering, Tianjin University, Tianjin 300072, China*

^b*University of Southern California, Los Angeles, CA 90089-2531, USA*

Abstract

The scattering of SV waves by a canyon in a fluid-saturated, poroelastic layered half-space is modeled using the indirect boundary element method in the frequency domain. The free-field responses are calculated to determine the displacements and stresses at the surface of the canyon, and fictitious distributed loads are then applied at the surface of the canyon in the free field to calculate the Green's functions for displacements and stresses. The amplitudes of the fictitious distributed loads are determined from the boundary conditions, and the displacements arising from the waves in the free field and from the fictitious distributed loads are summed to obtain the solution. The effects of fluid saturation, boundary conditions, porosity, and soil layers on the surface displacement amplitudes and phase shifts are discussed, and some useful conclusions are obtained. It is shown that the surface displacement amplitudes due to saturation and boundary conditions, different porosities, or the presence of a soil layer can be very dissimilar, and large phase shifts can be observed. The resulting wavelengths for an undrained saturated poroelastic medium are slightly longer than those for a drained saturated poroelastic medium; and are longer for a drained saturated poroelastic medium than those for a dry poroelastic medium. As porosity increases, the wavelengths become longer; and a layered half-space produces longer wavelengths than a homogeneous half-space.

© 2006 Elsevier Ltd. All rights reserved.

1. Introduction

The effect of local site conditions on seismic wave propagation is a fundamental subject in seismology and earthquake engineering. These problems can be solved by numerical or analytical methods. Analytical solutions are restricted to surface and sub-surface topographies with geometrically simple cross sections (e.g. circular, elliptical) in a homogeneous half-space [1–6]. More general cases must be analyzed numerically (e.g. [7–14]). In particular, Wolf [12], following Luco and Apsel [15], derived the exact dynamic-stiffness matrices and Green's functions of a layered half-space. These results comprise a complete theory of wave propagation and dynamic soil–structure interaction, which has been widely used by the engineering community. However, in reality, soil is not homogeneously elastic, but poroelastic and often saturated with fluid,

especially in coastal areas. Wolf's theory cannot be directly applied to wave propagation in a poroelastic medium, and therefore extending their work to deal with poroelasticity is a significant goal.

The theory of elastic wave propagation in a fluid-saturated poroelastic medium was first formulated and presented by Biot [16–18] and, more recently, the dynamic-stiffness matrices and Green's functions have been developed for a layered fluid-saturated poroelastic soil medium (e.g. [19–23]). However, solutions for wave diffraction involving a fluid-saturated poroelastic half-space medium are limited to certain simple site configurations and conditions.

In this paper, we start with Biot's equations [18], and is here to analyze the scattering of SV waves by a canyon in a horizontally layered fluid-saturated half-space. To do this, we use the indirect boundary element method (IBEM) in the frequency domain, with dynamic-stiffness matrices [22] that correspond to a layered fluid-saturated soil, and Green's functions [23], which represent distributed loads or pore pressure acting on an inclined line segment in a poroelastic layered half-space.

*Corresponding author.

E-mail addresses: liang@tju.edu.cn (J. Liang), vlee@usc.edu (V.W. Lee).

The purpose of this paper is to illustrate and verify this new method in comparison with related solutions. We will illustrate the simple dependency of our results on material properties, boundary conditions, and on the presence or absence of fluid in the porous medium. Detailed studies of the physical nature of soil motion, and how this depends on the properties of porous material, will be presented in future papers.

2. Methodology

We use the IBEM to determine the wave scattering around a canyon in a horizontally layered fluid-saturated half-space (Fig. 1). The IBEM in the frequency domain is applied in this study.

We begin with the calculation of the free-field response. From this, we can determine the horizontal and vertical displacements of the solid frame, $U_x(s), U_z(s)$, the displacement, $w(s)$, of the pore fluid with respect to the solid phase, the horizontal and vertical stresses, $t_x(s), t_z(s)$, in the solid frame, and the pore pressure, $t_p(s)$, at the surface of the canyon. Fig. 1 shows the positions and orientations of the displacement and stress vectors. Next, horizontal and vertical distributed fictitious source loads ($p(s), r(s)$) are applied at the surface of the canyon in the free field, and a pore pressure fictitious source load ($q(s)$) is also applied. Fig. 2 shows the positions and orientations of the applied fictitious source loads. The corresponding Green’s functions for the displacements and stresses are then calculated. The

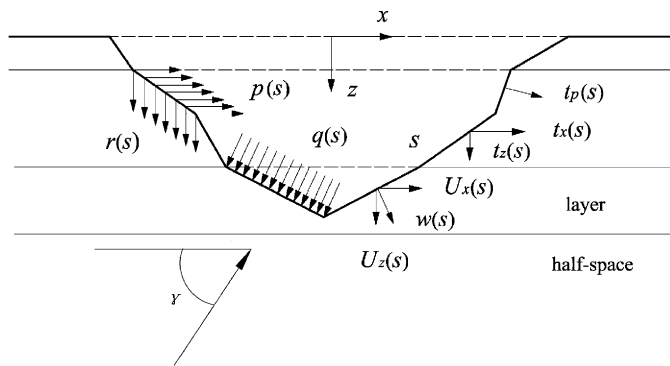


Fig. 1. Discretization of the canyon surface.

amplitudes of the fictitious source loads are determined by setting the boundary conditions at which the stresses and the pore pressure (or the displacement of pore fluid with respect to solid phase), arising from the waves in the free field and from the fictitious loads on the canyon’s surface, vanish. These boundary conditions can be satisfied in an averaged sense by using the method of weighted residuals.

We use Green’s function for the linearly distributed loads acting on an inclined line in a poroelastic layered half-space, which allows us to find the dynamic-stiffness matrix of a poroelastic layered half-space. The details of this approach are presented in previous works of [22,23]. The procedures will only be summarized briefly here.

On the basis of Biot’s equation, the general solution of the wave equation can be deduced by introducing the wave potential functions, allowing the exact dynamic-stiffness matrices of a poroelastic soil layer and a poroelastic half-space to be derived. The global stiffness matrix of a multi-layered site is then assembled from the layered and half-space stiffness matrices while considering the boundary conditions at the interfaces between the layers. Using the integral transform method, the Green’s functions of a distributed load or pore pressure acting on the horizontal, vertical and inclined lines in a poroelastic layered site can then be derived. These procedures extend Wolf’s theory from an elastic layered half-space to a poroelastic layered half-space. This formalism allows the key problems in wave propagation and dynamic soil–structure interaction to be resolved using the indirect boundary element method. This approach has the following advantages: all parameters in the dynamic-stiffness matrices have explicit physical meanings, the computational precision is not influenced by the thickness of the sub-layers, and depending on the parameters given, the stiffness matrices can be reduced to either the elastic or the dry poroelastic case.

2.1. Biot’s equation

The equations of motion [18] of a poroelastic medium can be expressed as

$$\mu \nabla^2 U + (\lambda_c + \mu) \text{grad}(\text{div } U) + \alpha M \text{grad}(\text{div } w) = \rho \ddot{U} + \rho_f \ddot{w}, \tag{1}$$

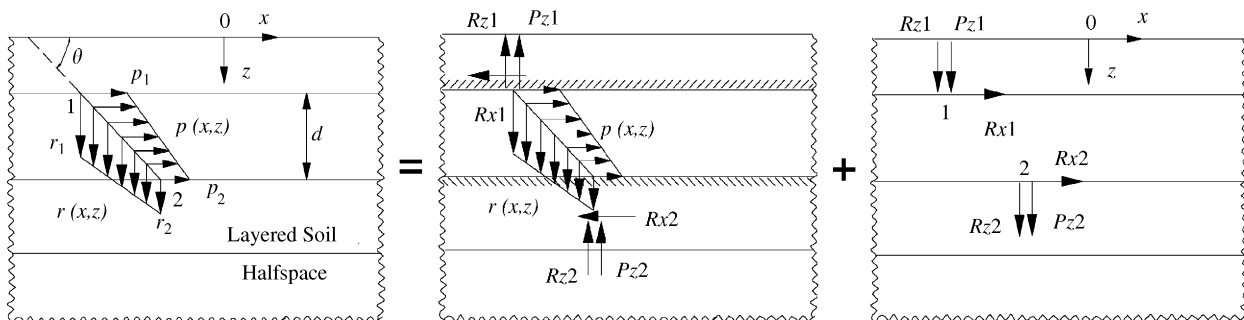


Fig. 2. Distributed load acting on an inclined line in soil layers.

$$\begin{aligned} &\alpha M \text{grad}(\text{div } U) + M \text{grad}(\text{div } w) \\ &= \rho_f \ddot{U} + m\dot{w} + b\dot{w}, \end{aligned} \quad (2)$$

where U and w are, respectively, the displacement vectors of the solid frame and the pore fluid with respect to the solid frame; ρ is the total density, $\rho = (1 - n)\rho_s + n\rho_f$; ρ_s and ρ_f are the densities of solid grains and of the pore fluid, n is the porosity; μ and λ are the Lamé constants of the bulk material; $\lambda_c = \lambda + \alpha^2 M$; α and M are the Biot's parameters, which account for compressibility of a two-phase material; m is a density-like parameter that depends on ρ_f and the geometry of the pores; and b is a parameter that accounts for internal friction due to relative motion between the solid frame and the pore fluid. In this paper, $m = \rho_f/n$ and $M = K_f/n$, where K_f is the bulk modulus of the pore fluid.

2.2. Free-field response

By assembling the dynamic-stiffness matrices and load vectors of the individual layers in the half-space, the equation of motion of a layered saturated poroelastic half-space can be expressed as

$$[S_{P1-P2-SV}]\{U\} = \{Q\}, \quad (3)$$

where $[S_{P1-P2-SV}]$ is the global stiffness matrix of the layered half-space [22], $\{U\}$ is the vector of the displacements, and $\{Q\}$ is the vector of the external loads. Solving this system gives the free-field responses, which consists of the in-plane free-field displacements of the solid in the x - and z -directions, the displacement of the pore fluid with respect to the solid phase $\{U_{xf}(s) \ U_{zf}(s) \ w_f(s)\}^T$, the resultant free-field stresses of the solid in the x - and z -direction and the pore pressure $\{t_{xf}(s) \ t_{zf}(s) \ t_{pf}(s)\}^T$ on the free surface of the canyon (Fig. 1). The subscript 'f' indicates that the variables represent terms in the free-field response.

2.3. Layered half-space Green's functions

In the case of a layered half-space, the Green's function denotes the dynamic response at any point in the free-field system when a unit load is applied somewhere in the system. Fig. 2 shows a distributed load acting on an inclined line in a soil layer. This version of Green's functions for a layered half-space originates from the work of Luco and Apsel [15]. The distributed loads $p(x, z)$ and $r(x, z)$, with their amplitudes p_1, p_2 and r_1, r_2 , are applied at the canyon surface, so that no singularity is introduced. At first, the two interfaces in each layer are assumed to be fixed, and the corresponding reaction forces R_{x1}, R_{z1}, P_{z1} and R_{x2}, R_{z2}, P_{z2} are calculated. The directions of these forces are then reversed, and they are applied as loads in the discretized equation of the layered half-space to determine the global response. The total response can then be found by adding the result of the analysis of fixed layers. More details of the Green's function that results from the

distributed loads and pore pressure can be found in You and Liang [23] or in You [24]. The latter is a dissertation in which the concepts formulated in Wolf [12]: "Dynamic Soil-Structure Interaction" is adopted. The Green's functions for a layered half-space, and the dynamic-stiffness matrices of the layered soil medium are taken and extended to the poroelastic case. The treatment will be briefly summarized as follows.

Calculations are performed in the wave-number domain, using the Green's functions in the space domain obtained by Fourier transformation of the displacements and stresses

$$\{U(s)\} = \int_{-\infty}^{+\infty} \{U(k)\} \exp(-iks) dk. \quad (4)$$

The resulting displacements and stresses at the canyon surface, S , can be expressed as

$$\begin{Bmatrix} U_{xg}(s) \\ U_{zg}(s) \end{Bmatrix} = [g_u(s)] \begin{Bmatrix} p \\ r \\ q \end{Bmatrix}, \quad (5)$$

$$\begin{Bmatrix} t_{xg}(s) \\ t_{zg}(s) \\ t_{Pg}(s) \end{Bmatrix} = [g_t(s)] \begin{Bmatrix} p \\ r \\ q \end{Bmatrix}, \quad (6)$$

where $[g_u(s)]$, $[g_t(s)]$ are the Green's functions for the drained boundary. In Eqs. (5) and (6), the subscript 'g' in the displacement terms $\{U_{xg}(s) \ U_{zg}(s)\}^T$ and the stress terms $\{t_{xg}(s) \ t_{zg}(s) \ t_{Pg}(s)\}^T$ indicates results attributable to the fictitious source loads.

Similarly,

$$\begin{Bmatrix} U_{xg}(s) \\ U_{zg}(s) \end{Bmatrix} = [g_{uu}(s)] \begin{Bmatrix} p \\ r \\ q \end{Bmatrix}, \quad (7)$$

$$\begin{Bmatrix} t_{xg}(s) \\ t_{zg}(s) \\ w_g(s) \end{Bmatrix} = [g_{tu}(s)] \begin{Bmatrix} p \\ r \\ q \end{Bmatrix}, \quad (8)$$

with $[g_{uu}(s)]$ and $[g_{tu}(s)]$ being the Green's functions that correspond to the undrained boundary. The elements in the vector $\{p(s), r(s), q(s)\}^T$ are the fictitious source loads in the x - and z - directions and the fictitious pore pressure along the canyon surface.

2.4. Boundary conditions

The conditions for a drained boundary of the canyon can now be expressed as

$$\int_S [W(s)]^T \left(\begin{Bmatrix} t_{xg}(s) \\ t_{zg}(s) \\ t_{Pg}(s) \end{Bmatrix} + \begin{Bmatrix} t_{xf}(s) \\ t_{zf}(s) \\ t_{pf}(s) \end{Bmatrix} \right) ds = 0 \quad (9)$$

with the weighting function $[W(s)]$. If $[W(s)]$ takes the value 1 in a single element and zero in all the others, the integral can be evaluated over each element separately. Substituting Eq. (6) into Eq. (9) gives

$$[T_p] \begin{Bmatrix} p \\ r \\ q \end{Bmatrix} = \{T_f\}, \tag{10}$$

with $[T_p] = \int_s [W(s)]^T [g_{tu}(s)] ds$ and $\{T_f\} = - \int_s [W(s)]^T \{t_{xf}(s) \ t_{zf}(s) \ t_{pf}(s)\}^T ds$.

Combining the solutions of Eqs. (10) and (5), the surface displacements of the canyon become

$$\begin{Bmatrix} U_x(s) \\ U_z(s) \end{Bmatrix} = \begin{Bmatrix} U_{xf}(s) \\ U_{zf}(s) \end{Bmatrix} + [g_{uu}(s)] [T_p]^{-1} \{T_f\}. \tag{11}$$

In a similar manner, the conditions for the undrained boundary of a canyon can be expressed as

$$\int_S [W(s)]^T \left(\begin{Bmatrix} t_{xg}(s) \\ t_{zg}(s) \\ w_g(s) \end{Bmatrix} + \begin{Bmatrix} t_{xf}(s) \\ t_{zf}(s) \\ w_f(s) \end{Bmatrix} \right) ds = 0. \tag{12}$$

Substituting Eq. (8) into Eq. (12) results in

$$[T_p] \begin{Bmatrix} p \\ r \\ q \end{Bmatrix} = \{T_f\}, \tag{13}$$

where $[T_p] = \int_s [W(s)]^T [g_{tu}(s)] ds$ and $\{T_f\} = - \int_s [W(s)]^T \{t_{xf}(s) \ t_{zf}(s) \ w_f(s)\}^T ds$.

Combining the solutions of Eq. (13) and (7), the surface displacements of the canyon become

$$\begin{Bmatrix} U_x(s) \\ U_z(s) \end{Bmatrix} = \begin{Bmatrix} U_{xf}(s) \\ U_{zf}(s) \end{Bmatrix} + [g_{uu}(s)] [T_p]^{-1} \{T_f\}. \tag{14}$$

The conditions for zero stress of a drained or undrained boundary at the surface of the half-space are satisfied automatically, since the free-field response and layered half-space Green's functions are obtained under the corresponding boundary conditions.

2.5. Numerical implementation

The free-field response can be calculated using Eq. (3), and the result will be exact in theory, since the dynamic-stiffness matrices for the soil layer and the half-space are both exact. However, computation of the Green's functions is a numerical process that is very time consuming. The numerical integration of Eq. (4) along the canyon surface, S , which determines the responses due to the fictitious source loads, can be performed in the wave-number domain over the wave number k within a large enough finite range, instead of the infinite range that would be required for an inverse Fourier transform. But it still requires a lot of arithmetic computations, which has to be performed very accurately. The maximum wave number k_{max} and the minimum integration interval Δk can be determined by numerical experiments. By depending on the

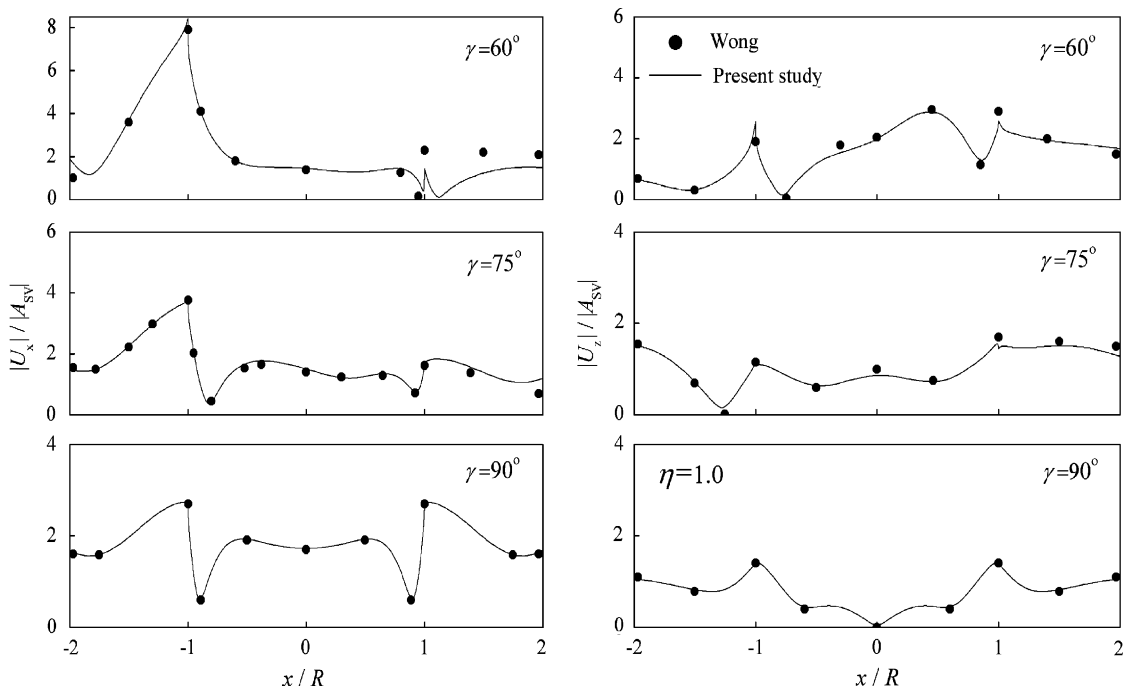


Fig. 3. Surface displacement amplitudes compared with those of Wong [10].

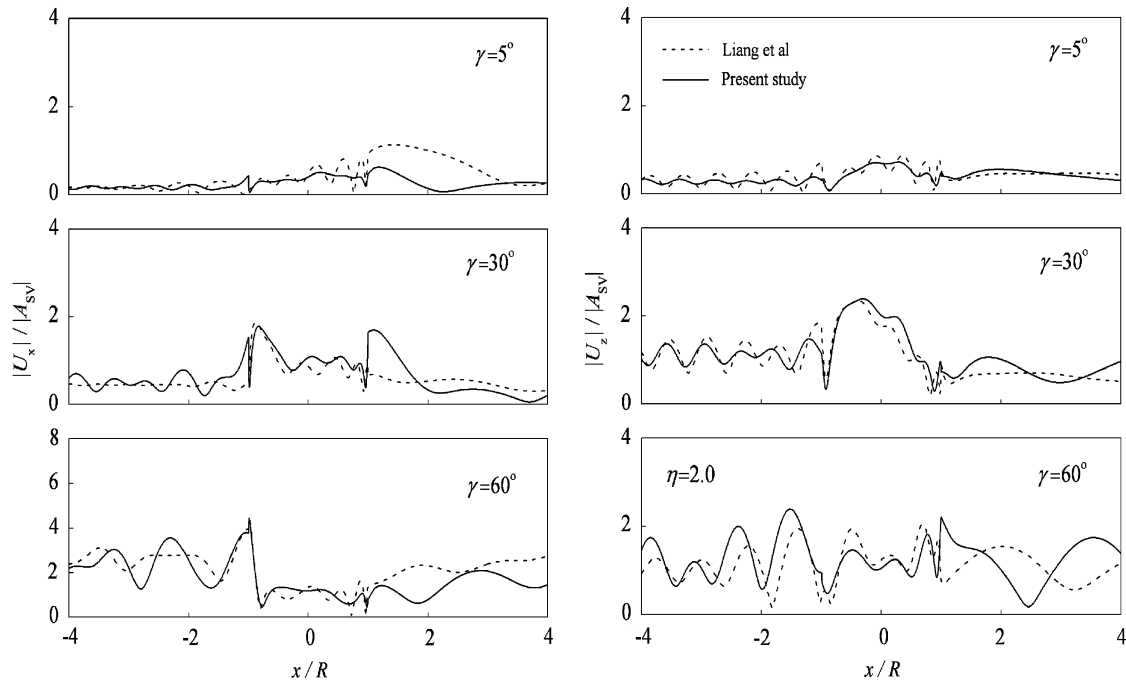


Fig. 4. Surface displacement amplitudes compared with those of Liang et al. [25].

incident frequencies, values of k_{max} up to 300–500, and minimum steps of $\Delta k = 0.0005-0.001$ are used. We solve the numerical integration of Eq. (4) by the method, Gaussian quadrature. This requires a small amount of material damping, which leads to a finite value of $U(k)$ for all values of k [12]. A material damping ratio of 0.001 was used in these calculations.

Another approximation made in our methodology is that the boundary conditions are satisfied numerically by the weighted residual method, through the discretization of the canyon surface. The extent to which accuracy is compromised will depend on the amount of discretization.

2.6. Verification

In the case of a dry poroelastic solid (no fluid, $\rho_f = 0$), the above model should match that of the elastic half-space studied by Wong [10]. Fig. 3 illustrates that this is indeed so for the scattering of SV waves by a semi-circular canyon in a homogeneous half-space. A dimensionless incident frequency is defined as $\eta = \omega R / \pi c_s$, where R is the radius of the semi-circular canyon, and c_s is the shear velocity of the dry poroelastic solid. $|U_x|$ and $|U_z|$ are the amplitudes of displacements in the x - and z -directions, $|A_{SV}|$ is the amplitude of the incident wave, and γ is the incident angle. The results of the present study agree well with those of Wong [10]. For the horizontal displacement amplitude ($|U_x|$) when $\gamma = 60^\circ$ and $x/R > 1$, the agreement is not so close.

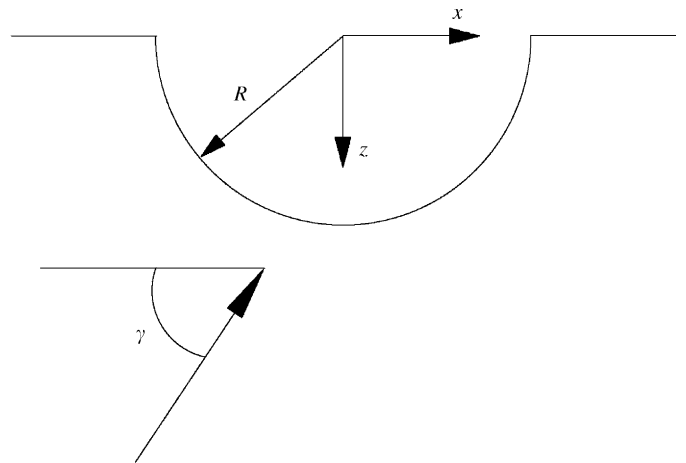


Fig. 5. A semi-circular canyon in a homogeneous half-space.

Fig. 4 shows the surface displacement amplitudes of a semi-circular canyon in a saturated poroelastic half-space compared with results for the same topography in Liang et al. [25], solved by the wave function expansion method. The parameters of the saturated poroelastic half-space are as follows: porosity $n = 0.3$, shear modulus $\mu = 2846$ Mpa, solid grain density $\rho_s = 2650 \text{ kg m}^{-3}$, pore fluid density $\rho_f = 1000 \text{ kg m}^{-3}$, Poisson's ratio $\nu = 0.3$, Biot's parameter $\alpha = 0.99$, internal friction parameter $b = 0$, $K_f = 2000$ MPa, $m = \rho_f / n$, and $M = K_f / n$, as defined in Section 2.1 above. A drained boundary condition is used in this example, and the dimensionless incident frequency is defined as

$\eta = \omega R / \pi \sqrt{\rho_s / \mu}$, where R is the radius of the semi-circular canyon. As before, $|U_x|$ and $|U_z|$ are the amplitudes of displacements in x - and z - directions, $|A_{SV}|$ is the amplitude of incident SV wave, and γ is the incident angle. Fig. 4 shows that our results are reasonably

satisfactory and consistent with those of Liang et al. [25]. But the results are not identical, largely because of the differences in the Biot's models in the two studies, and there may also lie some effects from the different approximations used.

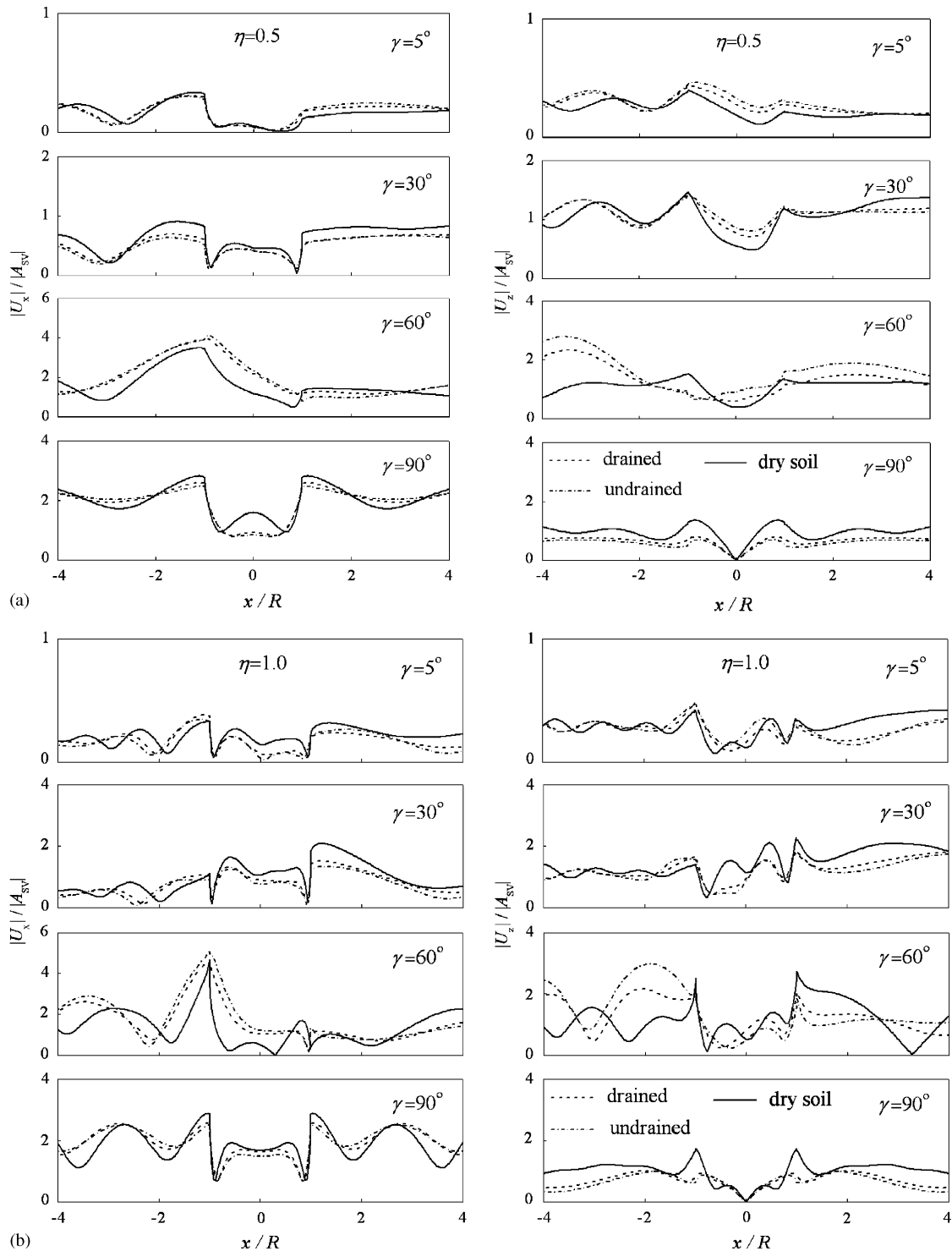


Fig. 6. Effect of fluid saturation and boundary conditions.

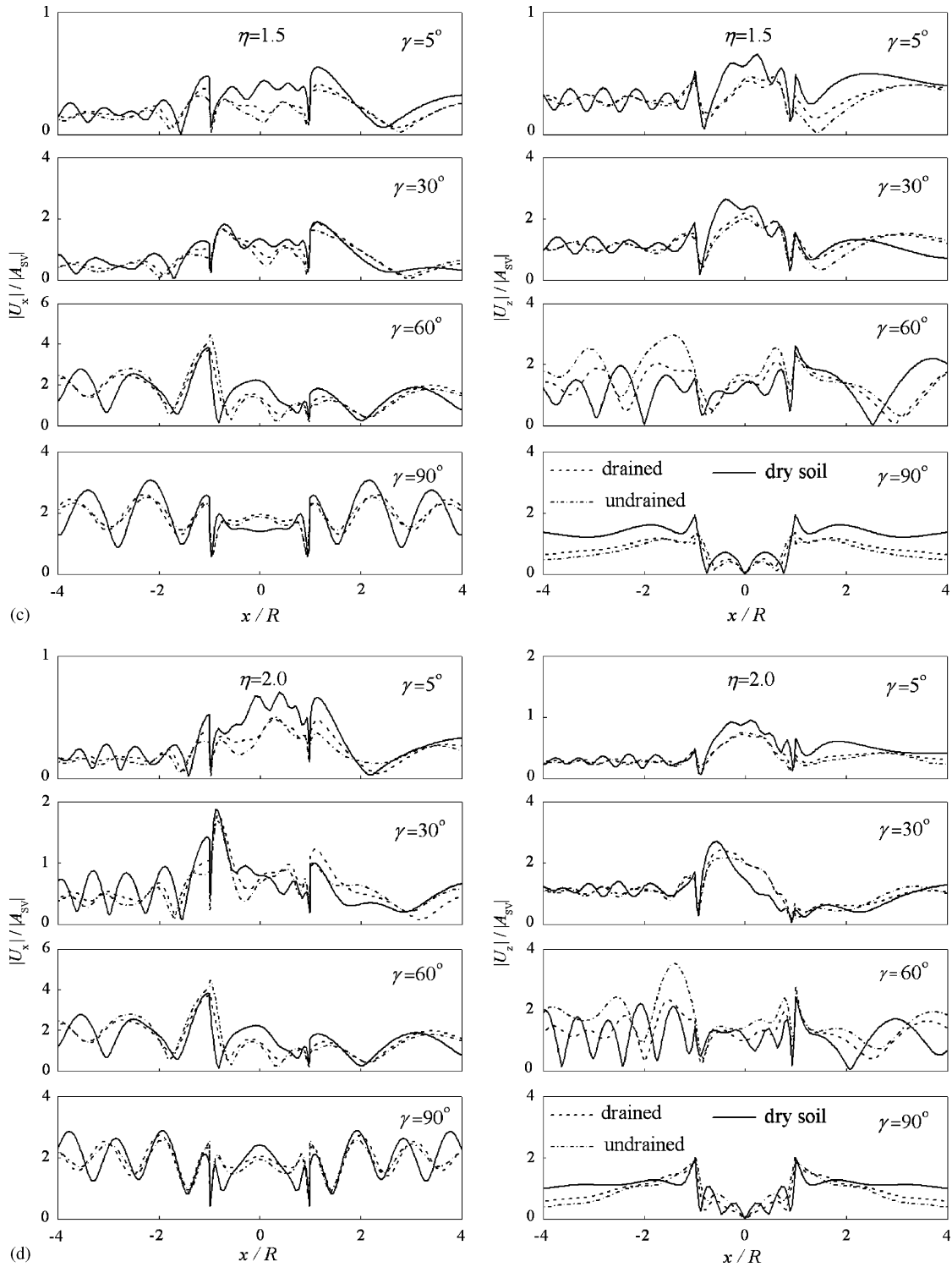


Fig. 6. (Continued)

3. Numerical results and discussion

3.1. Effect of fluid saturation and boundary conditions

We now analyze a semi-circular canyon in a fluid-saturated homogeneous half-space (Fig. 5). A saturated

poroelastic medium with drained and undrained boundary conditions and the relevant dry poroelastic medium are studied. The material parameters, as defined above, are as follows: $n = 0.375$, $\mu = 183 \text{ MPa}$, $\rho_s = 2650 \text{ kg m}^{-3}$, $\rho_f = 1000 \text{ kg m}^{-3}$, $\nu = 0.25$, $\alpha = 0.99$, $b = 1.0 \text{ MPa s m}^{-4}$, $m = 2667 \text{ kg m}^{-3}$, $M = 5600 \text{ MPa}$. Material damping is taken to

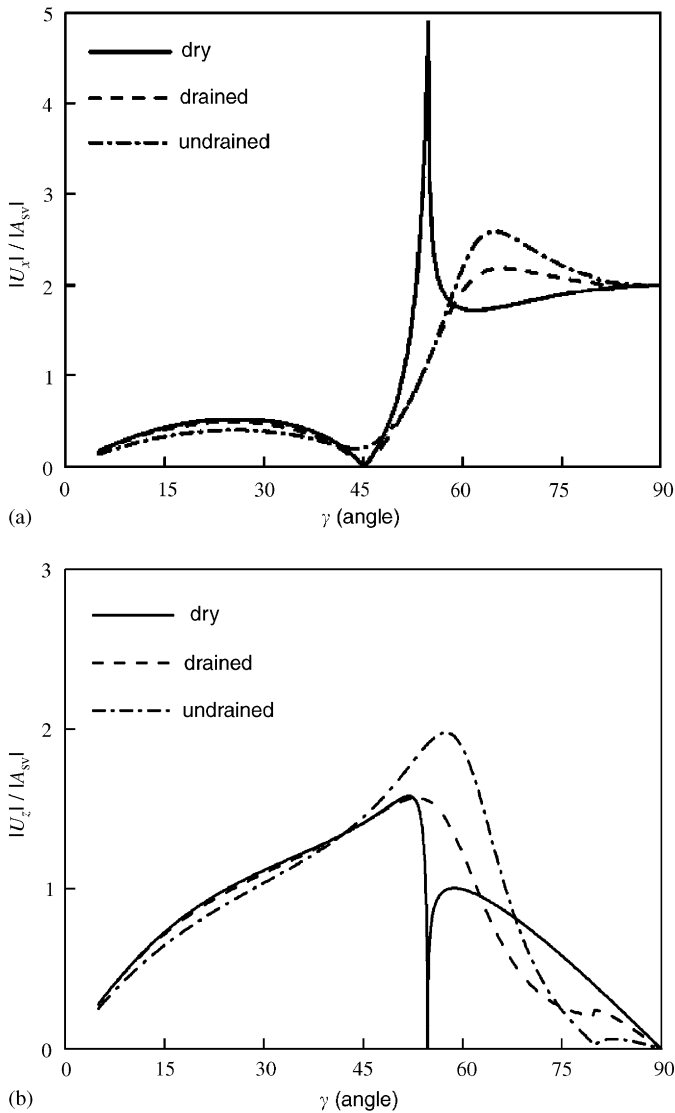


Fig. 7. Surface displacement amplitudes of a free-field half-space.

be 1% in the numerical calculations. We define the dimensionless incident frequency as $\eta = \omega R / \pi \sqrt{\rho_s / \mu}$, where R is the radius of the semi-circular canyon. Fig. 6 illustrates the surface displacement amplitudes for dimensionless incident frequencies η of 0.5, 1.0, 1.5 and 2.0, $|U_x|$ and $|U_z|$ are again the amplitudes in x - and z -directions, respectively, $|A_{SV}|$ is the amplitude of incident wave, and γ is the incident angle.

These figures show that the surface displacement amplitudes of saturated and dry poroelastic medium can be very different, depending on the dimensionless frequencies, the incident angles, and the surface positions (x/R), and obvious phase shifts can be observed. The differences may be due to a combination of the free-field effect and the canyon effect, which both depend strongly on the incident angles.

To illustrate the free-field effect, Fig. 7 shows the surface displacement amplitudes versus incident angles for the

relevant saturated poroelastic half-spaces and for the dry poroelastic half-space without the canyon. It can be seen that, with an incident angle of $\gamma = 60^\circ$, both the horizontal and vertical displacement amplitudes are largest for the undrained half-space, second largest for the drained half-space, and smallest for the dry half-space; while for other incident angles $\gamma = 5^\circ, 30^\circ$ and 90° , the displacement amplitudes are almost identical for the undrained, drained and dry half-spaces.

The results show in Fig. 6, with the canyon present, large surface displacement amplitudes occur around the left rim ($x/R = -1$) of the canyon at the incident angle of $\gamma = 60^\circ$. Also, both the horizontal and vertical displacement amplitudes are again largest for the undrained poroelastic medium, second largest for the drained poroelastic medium, and smallest for the dry poroelastic medium. This agrees with the corresponding free-field displacements, and may be explained by the different free-field motions illustrated above. We might then reasonably conclude that the differences in surface displacement amplitudes for other incident angles $\gamma = 5^\circ, 30^\circ$ and 90° are due to the canyon effect.

It can be seen from Fig. 6 that the wavelengths of the waves in the undrained saturated poroelastic medium are slightly longer than those of the drained saturated poroelastic medium, and the wavelengths in the drained saturated poroelastic medium are longer than those of the dry poroelastic medium. These differences may be due to wave interference around the canyon. Overall, it is reasonable to assert that fluid saturation and boundary conditions have significant influence on the response of a canyon subjected to incident SV waves.

3.2. Effect of porosity and skeleton stiffness

Fig. 8 illustrates the surface displacement amplitudes around a semi-circular canyon in a homogeneous saturated poroelastic half-space under drained boundary condition for different porosities $n = 0.1, 0.3$ and 0.34 . Sandstones with a linear porosity–elastic modulus relation [26] are chosen for the following numerical analysis, and the corresponding shear modulus for the dry solid are $\mu = 12030, 2846$ and 1010 MPa, respectively. Other material parameters of the saturated poroelastic half-space, as defined above, are given as follows: solid grain density $\rho_s = 2650 \text{ kg m}^{-3}$, pore fluid density $\rho_f = 1000 \text{ kg m}^{-3}$, $\nu = 0.3$, $\alpha = 0.99$, $b = 0$, $K_f = 2000$ MPa, $m = \rho_f/n$, and $M = K_f/n$. The dimensionless incident frequency is again defined as $\eta = \omega R / (\pi \sqrt{\mu / \rho_s})$, with R being the radius of the semi-circular canyon.

Fig. 8 shows that large differences for the surface displacement amplitudes, depending on different porosities, and large phase shifts can be observed. Large horizontal amplitudes occur near the left corner ($x/R = -1$) for an incident angle $\gamma = 60^\circ$, which may be due to the larger horizontal amplitudes of the free-field

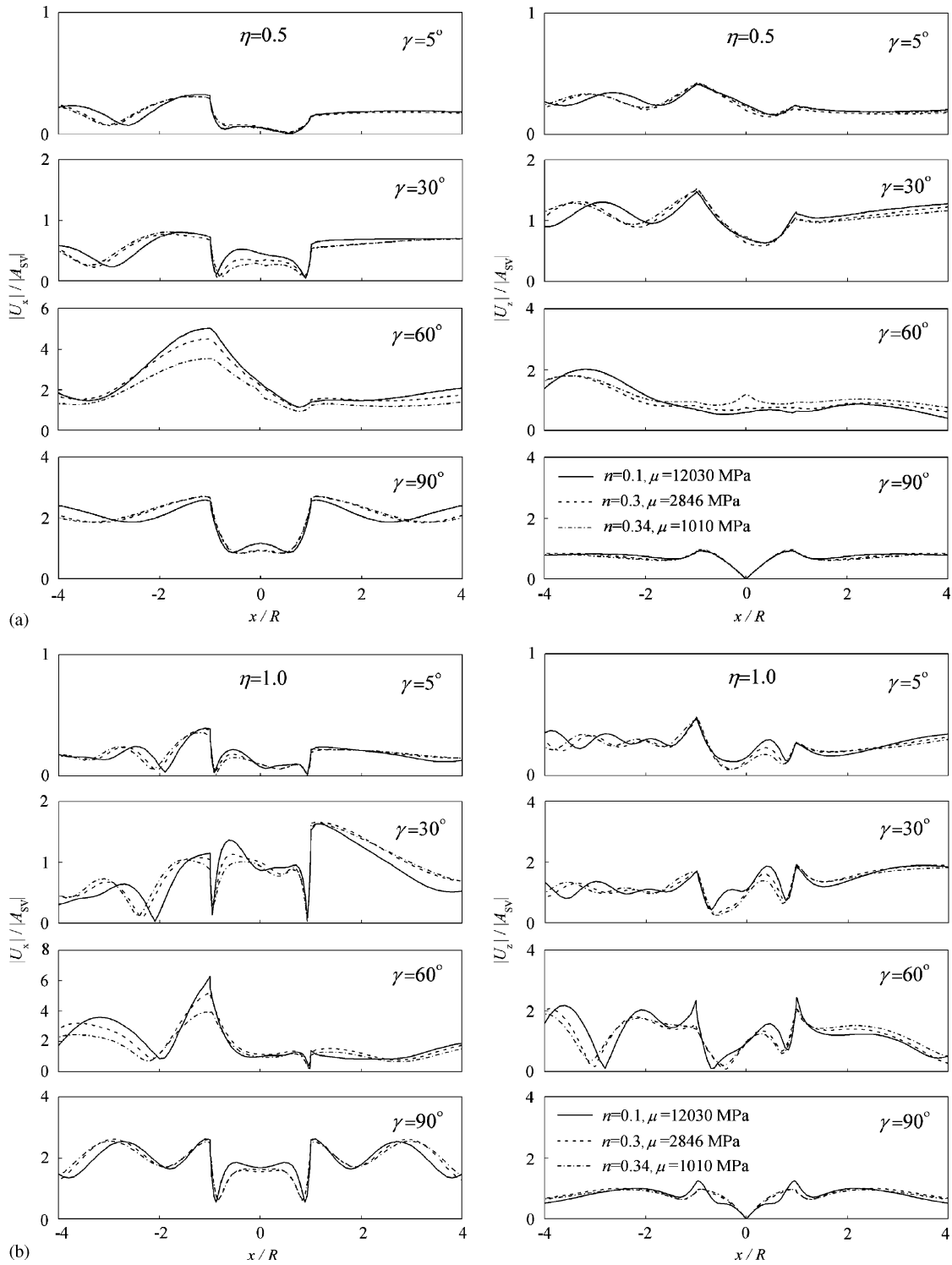


Fig. 8. Effect of porosity and skeleton stiffness.

response for smaller porosities at $\gamma = 60^\circ$ [26]; as the porosity increases, the resulting wavelengths become longer. We conclude that porosity has significant effect on wave scattering around a canyon in a saturated poroelastic half-space.

3.3. Effect of a layered half-space

A semi-elliptical canyon in a layered saturated poroelastic half-space (Fig. 9) is studied next. For simplicity, we use a model consisting of one layer over a half-space; this

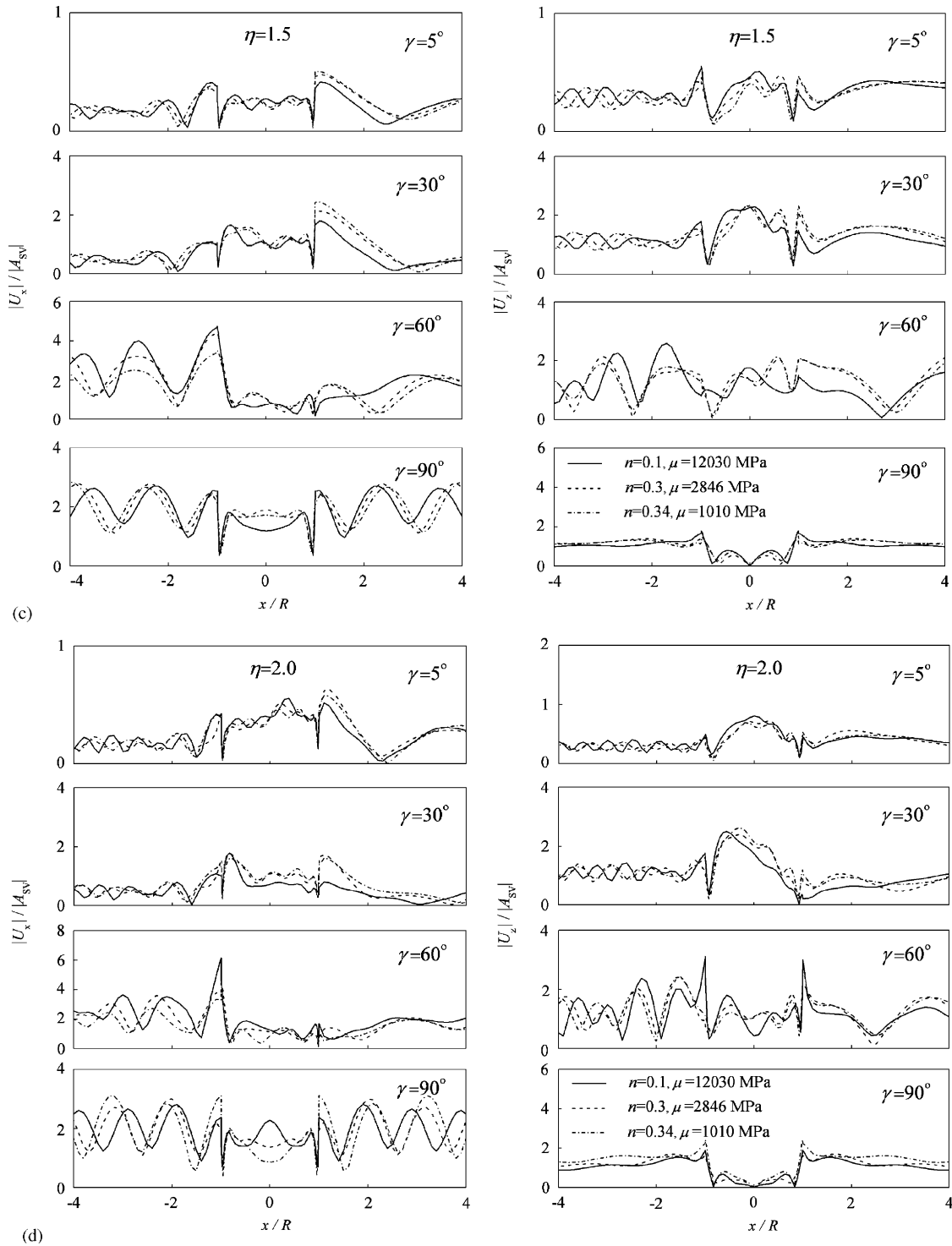


Fig. 8. (Continued)

represents the simplest layered half-space. The thickness of the soil layer is D , and the long and short axes of the ellipse are $A = 1.5D$ and $B = D$. The density of the pore fluid is $\rho_f = 1000 \text{ kg m}^{-3}$, and other parameters of the layer and the half-space are given in Table 1. The dimensionless incident frequency is again defined as $\eta = \omega A / \pi \sqrt{\rho_s / \mu}$,

where μ and ρ_s are the shear modulus and solid grain density of the half-space. Both the soil layer and the half-space are saturated, and we use a drained boundary condition here.

Fig. 10 illustrates the surface displacement amplitudes around the semi-elliptical canyon in the saturated

layered half-space and in the saturated homogeneous half-space. The saturated homogeneous half-space is characterized by the parameters of the half-space in Table 1. In Fig. 10, $|U_x|$ and $|U_z|$ are the surface displacement amplitudes in the x - and z -directions, $|A_{SV}|$ is the amplitude of the incident wave, and γ is the incident angle.

It is shown that the surface displacement amplitudes can differ greatly between the layered half-space and the homogeneous half-space, depending on the dimensionless frequencies and incident angles, and large phase shifts are observed.

To explain these differences, the corresponding free-field response for the saturated layered half-space and for the saturated homogeneous half-space are plotted in Fig. 11. Table 2 gives the actual numerical maximum amplitudes for dimensionless incident frequencies η of 0.5, 1.0, 1.5 and 2.0. From Fig. 11 and Table 2, it can be seen that the surface displacement amplitudes for the layered half-space are highly dependent on both the incident angles and the incident frequencies. But such dependencies is less for the homogeneous half-space, because of the resonances in the layered half-space. It is easy to see the regions of resonance in Fig. 11.

Fig. 10 shows that, when the frequency of the incident waves is near a resonant frequency of the layer, there are significant overall differences (even far from the canyon) between the surface displacement amplitudes for the layered half-space and for the homogeneous half-space. For instance, the maximum horizontal surface displacement amplitudes are 3.466 and 4.142, for the

layered half-space for $\gamma = 60^\circ$ at $\eta = 1.5$ and 2.0, respectively. However, the corresponding maximum amplitudes for the homogeneous half-space are only 0.365 and 1.138. Similarly, the maximum horizontal surface displacement amplitude is 4.778 for the layered half-space at $\gamma = 90^\circ$ and $\eta = 1.0$, but the corresponding amplitude for the homogeneous half-space is only 2.468. When the frequency of the incident wave is outside the resonant regions, the difference between the surface displacement amplitudes for the layered half-space and for the homogeneous half-space is usually not great. For example, this is the case for the vertical surface displacement amplitudes when $\gamma = 5^\circ$, $\eta = 1.0$, and $\gamma = 30^\circ$, $\eta = 0.5$, etc. Nonetheless, in some cases, the difference can still be very large, usually at points close to the canyon (caused by the canyon interference effect). For instance, the maximum horizontal surface displacement amplitude is 3.862 for the layered half-space when $\gamma = 60^\circ$, $\eta = 2.0$, but the corresponding horizontal surface displacement amplitude for the homogeneous half-space reaches 6.366. We can summarize by stating that the surface displacement amplitudes of a layered half-space depend not only on the ratio of the canyon width to the incident wavelength but also on the free-field resonant frequency.

It can also be seen from Fig. 10 that, depending on the incident angles and dimensionless incident frequencies, large phase shifts can occur and result in waves with longer wavelengths in the layered half-space than those in the homogeneous half-space. For instance, at the location of $x/A < -1.0$ for horizontal displacements, when $\gamma = 60^\circ$ and 90° , $\eta = 1.0, 1.5$ and 2.0. This is due to resonances in the layered half-space.

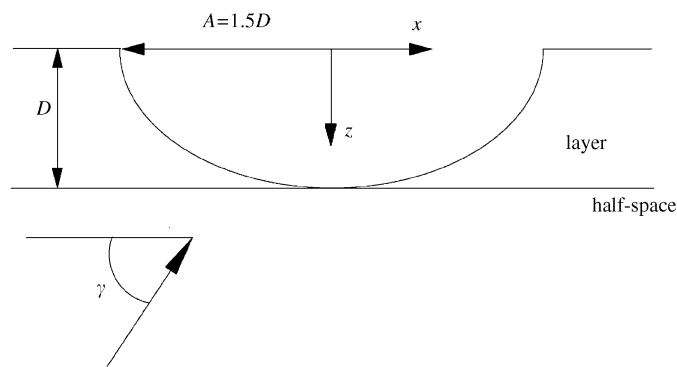


Fig. 9. A semi-elliptical canyon in a layered half-space.

4. Conclusions

The scattering of SV waves by a canyon in a fluid-saturated, poroelastic layered half-space is studied by an indirect boundary element method in the frequency domain. The free-field responses are calculated to determine the displacements and stresses at the surface of the canyon, and fictitious distributed loads are then applied at the surface of the canyon in the free field to calculate the Green's functions for the displacements and stresses. The amplitudes of the fictitious distributed loads are subsequently determined by the boundary conditions, and the displacements arising from the waves

Table 1
Parameters for a saturated layer and a saturated half-space

	μ (MPa)	λ (MPa)	M (MPa)	ρ_s (kg m ⁻³)	m (kg m ⁻³)	b (MPa s m ⁻⁴)	α
Half-space	1000	1000	2000	2400	4800	4.5	0.9
Soil layer	250	500	2500	2000	3000	1.5	0.95

in the free field and from the fictitious distributed loads are summed to obtain the solution. The effects of fluid saturation, boundary conditions, porosity, and soil layers on the surface displacement amplitudes and phase shifts are discussed, and some useful conclusions are obtained.

It is shown that the surface displacement amplitudes due to saturation and boundary conditions, different porosities, or the presence of a soil layer can be very dissimilar, and significant phase shifts can be observed. The resulting wavelengths in an undrained saturated poroelastic medium are slightly longer than

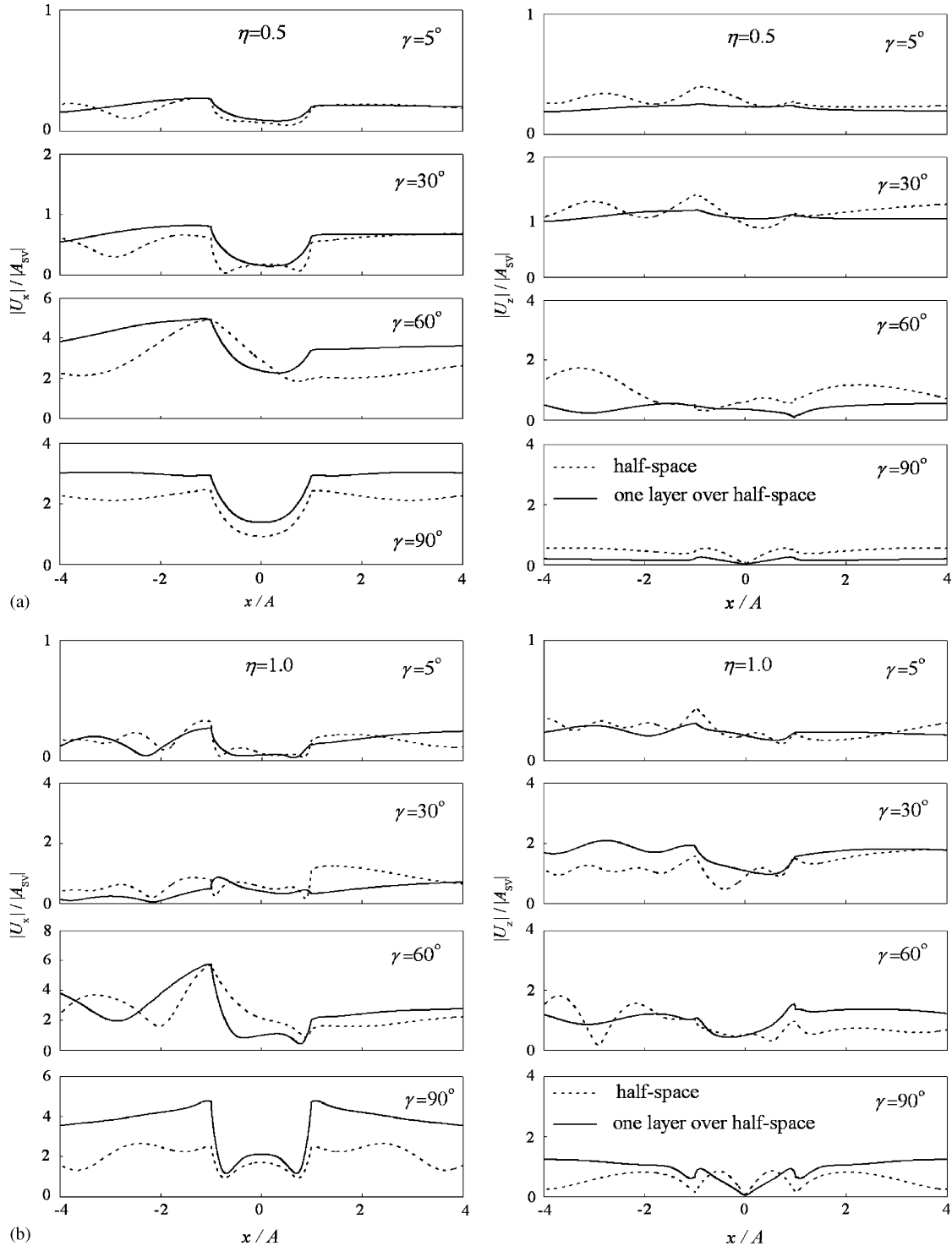


Fig. 10. Effect of a layered half-space.

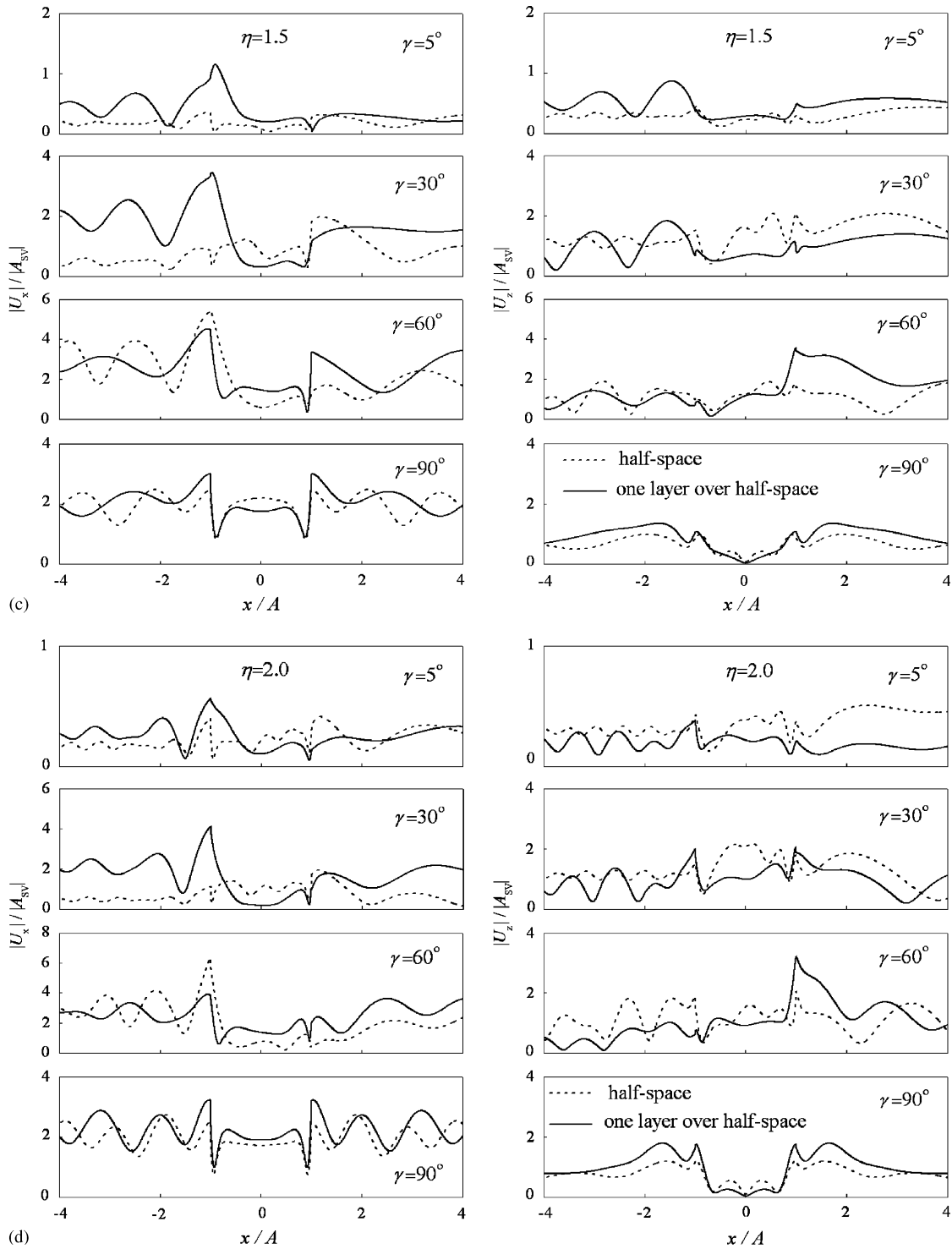


Fig. 10. (Continued)

those in a drained saturated poroelastic medium, and the resulting wavelengths in a drained saturated poroelastic medium are longer than those in a dry poroelastic medium. As the porosity increases, resulting wavelengths become longer; with those of the layered half-space are longer than those of the homogeneous half-space.

The method we have presented has been applied to circular and elliptical canyons, so that comparisons can be made with existing solutions for a dry half-space. The new method can also be used to describe wave scattering by a canyon of arbitrary shape in a layered fluid-saturated half-space. This will be discussed in a future paper.

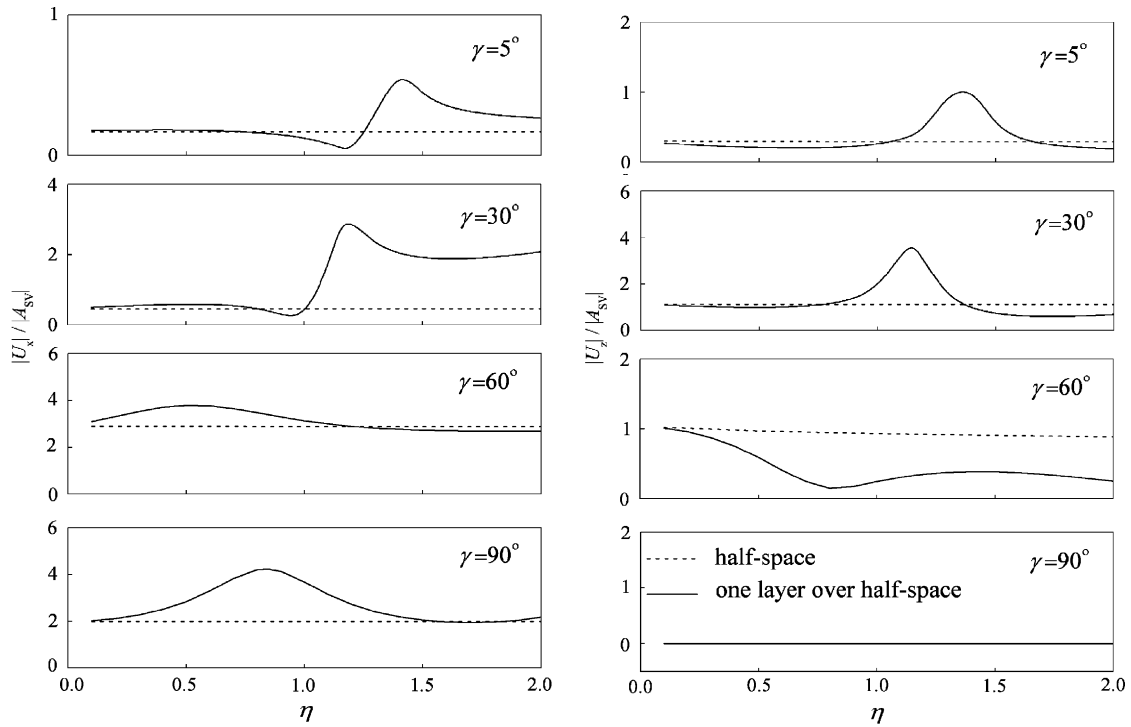


Fig. 11. Free-field response of a half-space and of a one layer over half-space versus dimensionless incident frequency.

Table 2
Free-field response of a half-space and a one layer over half-space for dimensionless incident frequencies $\eta = 0.5, 1.0, 1.5$ and 2.0

		$\eta = 0.5$		$\eta = 1.0$		$\eta = 1.5$		$\eta = 2.0$	
		Half-space	One layer over half-space	Half-space	One layer over half-space	Half-space	One layer over half-space	Half-space	One layer over half-space
$\gamma = 5^\circ$	$ U_x / A_{SV} $	0.168	0.181	0.168	0.126	0.168	0.428	0.168	0.267
	$ U_z / A_{SV} $	0.295	0.205	0.292	0.253	0.291	0.512	0.290	0.188
$\gamma = 30^\circ$	$ U_x / A_{SV} $	0.453	0.585	0.456	0.165	0.458	1.909	0.460	2.079
	$ U_z / A_{SV} $	1.120	0.988	1.118	1.863	1.116	0.721	1.115	0.686
$\gamma = 60^\circ$	$ U_x / A_{SV} $	2.901	3.793	2.897	3.140	2.896	2.724	2.896	2.695
	$ U_z / A_{SV} $	0.969	0.587	0.932	0.245	0.906	0.385	0.885	0.247
$\gamma = 90^\circ$	$ U_x / A_{SV} $	2.000	2.846	2.000	3.677	2.000	2.047	2.000	2.174
	$ U_z / A_{SV} $	0.000	0.000	0.000	0.000	0.000	0.000	0.000	0.000

Acknowledgements

The authors gratefully acknowledge the support of the National Natural Science Foundation of China under Grant no. 50378063. The authors are also very appreciative of the comments and suggestions from reviewers.

References

[1] Trifunac MD. Scattering of plane SH waves by a semi-cylindrical canyon. *Earthquake Eng Struct Dynam* 1973;1:267–81.

[2] Wong HL, Trifunac MD. Scattering of plane SH-waves by a semi-elliptical canyon. *Earthquake Eng Struct Dynam* 1974;3: 157–69.

[3] Cao H, Lee VW. Scattering of plane SH waves by circular cylindrical canyons with variable depth-to-width. *Eur J Earthquake Eng* 1989; 3(2):29–37.

[4] Lee VW, Cao H. Diffraction of SV waves by circular canyons of various depths. *J Eng Mech ASCE* 1989;115(9):2035–56.

[5] Cao H, Lee VW. Scattering of plane P waves by circular cylindrical canyons with various depth-to-width ratio. *Soil Dynam Earthquake Eng* 1990;9(3):141–50.

[6] Yuan X, Liao Z. Scattering of plane SH waves by a cylindrical canyon of circular-arc cross-section. *Soil Dynam Earthquake Eng* 1994;13:407–12.

- [7] Bouchon M. Effect of topography on surface motion. *Bull Seismol Soc Am* 1973;63:615–32.
- [8] Wong HL, Jennings PC. Effect of canyon topography on strong ground motion. *Bull Seismol Soc Am* 1975;65:1239–57.
- [9] Sanchez-Sesma FJ, Rosenblueth E. Ground motion at canyons of arbitrary shape under incident SH waves. *Earthquake Eng Struct Dynam* 1979;7:441–50.
- [10] Wong HL. Effect of surface topography on the diffraction of P, SV, and Rayleigh waves. *Bull Seismol Soc Am* 1982;72(4):1167–83.
- [11] Sanchez-Sesma FJ, Bravo MA, Herrera I. Surface motion of topographical irregularities for incident P, SV and Rayleigh waves. *Bull Seismol Soc Am* 1985;75:263–9.
- [12] Wolf JP. *Dynamic soil-structure interaction*. Englewood Cliffs, NJ: Prentice-Hall; 1985.
- [13] Kawase H. Time-domain response of a semi-circular canyon for incident SV, P and Rayleigh waves calculated by the discrete wave number boundary element method. *Bull Seismol Soc Am* 1988;78:1415–37.
- [14] Vogt RF, Wolf JP, Bachmann H. Wave scattering by a canyon of arbitrary shape in a layered half space. *Earthquake Eng Struct Dynam* 1988;16:803–12.
- [15] Luco J, Apsel R. On the Green's functions for a layered half-space. Part I. *Bull Seismol Soc Am* 1983;4:909–29.
- [16] Biot MA. The theory of propagation of elastic waves in a fluid-saturated porous solid: I. Low-frequency range. *J Acoust Soc Am* 1956;28:168–78.
- [17] Biot MA. The theory of propagation of elastic waves in a fluid-saturated porous solid: II. Higher-frequency range. *J Acoust Soc Am* 1956;28:179–91.
- [18] Biot MA. Mechanics of deformation and acoustic propagation in porous media. *J Appl Phys* 1962;33:1482–98.
- [19] Senjuntichai T, Rajapakse RKND. Dynamic Green's functions of homogeneous poroelastic half plane. *J Eng Mech ASCE* 1994;120(11):2381–404.
- [20] Philippacopoulos AJ. Spectral Green's dyadic for point sources in poroelastic media. *J. Eng. Mech.* 1998;124(1):24–31.
- [21] Pan E. Green's functions in layered poroelastic half-space. *Int. J. Num. Anal. Meth. Geomech* 1999;23:1631–53.
- [22] Liang J, You H. Dynamic stiffness matrix of a poroelastic multi-layered site and its Green's functions. *Earthquake Eng Eng Vib* 2004;3(2):273–82.
- [23] You H, Liang J. Green's functions for linearly distributed loads acting on inclined line in poroelastic layered site. *J Vib Eng* 2005;18(3):335–41.
- [24] You H. Elastic wave scattering by a canyon or cavity in layered saturated half-space. Ph.D. dissertation, Tianjin University, 2005.
- [25] Other-Ref: Liang J, Ba Z, Lee VW. Diffraction of plane SV waves by a shallow circular-arc canyon in a saturated poroelastic half-space. *Soil Dynam Earthquake Eng*, in press, doi:10.1016/j.solidyn.2006.01.011.
- [26] Lin CH, Lee VW, Trifunac MD. The reflection of plane waves in a poroelastic half-space fluid saturated with inviscid fluid. *Soil Dynam Earthquake Eng* 2005;25:205–23.